

1   **Lifespan of mountain ranges scaled by feedbacks between landsliding and erosion by**  
2   **rivers**

3

4   David L. Egholm<sup>1\*</sup>, Mads F. Knudsen<sup>1</sup>, Mike A. Sandiford<sup>2</sup>

5   <sup>1</sup>Department of Geoscience, Aarhus University, Høegh-Guldbergs Gade 2, 8000 Aarhus C.,  
6   Denmark

7   <sup>2</sup>School of Earth Sciences, University of Melbourne, Victoria, 3010, Australia

8   \*Correspondence to: david@geo.au.dk

9

10   **A particular challenge in tectonic geomorphology has been reconciling the high**  
11   **fluvial incision rates observed in tectonically active mountain ranges with the long-**  
12   **term ( $10^8$  years) preservation of significant topographic relief in ancient, tectonically**  
13   **inactive orogenic belts<sup>1-3</sup>.** While river bedrock erosion and sediment transport is  
14   widely recognised as the principal control on the lifespan of mountain ranges, the  
15   factors scaling the rate of erosion<sup>4-8</sup>, and the reasons they appear to vary significantly  
16   as function of tectonic activity, remain controversial. Using computational  
17   simulations, we show the key to understanding this paradox may relate to the two-  
18   way coupling between bedrock river incision and landslides. Importantly, while  
19   fluvial incision steepens surrounding hillslopes and increases landslide frequency<sup>9</sup>,  
20   landsliding impacts fluvial erosion rates in two fundamentally distinct ways. On the  
21   one hand, large landslides overwhelm the river transport capacity and cause

22 upstream aggradation of sediment that armors the riverbed from further erosion<sup>9-11</sup>.  
23 On the other hand, in delivering abrasive agents to the streams<sup>4-6</sup>, landslides help  
24 accelerate fluvial erosion. Our models illustrate how this coupling has fundamentally  
25 different implications for rates of fluvial incision in active and inactive mountain  
26 ranges, thereby providing a plausible physical explanation for the persistence of  
27 significant relief in old orogenic belts, up to several hundred-million-years after  
28 tectonic activity has effectively ceased.

29

30 The erosive power of rivers incises bedrock in mountain belts and forms self-organizing  
31 patterns characteristic of dendritic drainage systems. Bedrock incision occurs by a  
32 combination of processes related to the transport of both water and sediment within the  
33 rivers<sup>4-8</sup>. The balance between these erosion processes is poorly understood and models for  
34 fluvial landscape evolution often rely on the assumption that river erosion rates scale with  
35 some measure of flow intensity, such as stream power<sup>12</sup> or shear stress<sup>13</sup>, which are both  
36 simple functions of local relief and water discharge. These models, collectively referred to  
37 as “stream-power models”, have found widespread favor in the modeling community, as  
38 they reproduce many features observed in natural landscapes<sup>12-15</sup>.

39 However, stream-power models do not adequately capture the role of mobile sediment in  
40 fluvial erosion, and a number of recent studies of long-term erosion rates based on field  
41 measurements, low-temperature thermochronology, and cosmogenic nuclides, show that  
42 variations in precipitation rate<sup>16-19</sup> and topographical relief<sup>20,21</sup>, and hence stream power,  
43 do not always account for the long-term erosion rate of bedrock landscapes. Instead,

44 measurements of average catchment denudation rates suggest that erosion is fast primarily  
45 where active tectonism constantly rejuvenates the topographic surface<sup>1,2,16,19-21</sup> but slow in  
46 many high-relief passive orogens<sup>1,2,22</sup>, which require non-linear couplings between relief,  
47 discharge, and erosion that are not easily explained by the stream-power concept. In  
48 particular, the long-term preservation of km-scale relief in ancient, tectonically inactive,  
49 Paleozoic orogenic belts, such as the Appalachians in the USA, the Ural mountains in Russia,  
50 and the Caledonian mountains in Greenland and Scandinavia (supplementary Fig. S1)  
51 seems directly at odds with the stream-power concept for river erosion. Although post-  
52 orogenic uplift processes related to mantle dynamics may possibly have influenced some of  
53 the Paleozoic orogenic belts, the lifespan of mountainous relief in these old orogenic belts  
54 remains a long-standing problem in Earth sciences<sup>3</sup>.

55

56 To more accurately embody the physics of erosional processes in rivers, Sklar & Dietrich<sup>5,23</sup>  
57 proposed a process-based formalism for bedrock incision by saltating sediment particles in  
58 a river. In this saltation-abrasion model, the erosion rate is a direct function of abrasion per  
59 particle impact multiplied by the frequency of impacts and a sediment-cover factor<sup>23</sup>  
60 (Methods). This model, which captures the complex role of sediment concentration for the  
61 bedrock erosion rate, is supported by recent catchment-scale observations<sup>24</sup> and  
62 longitudinal river profiles<sup>25,26</sup>, but have yet to be tested against long-term landscape  
63 evolution at orogenic scales.

64

65 To explore the fundamental implications of feedbacks between hillslope erosion, sediment  
66 delivery, and channel incision in a non-glacial setting, we performed computational  
67 experiments that couple the full physics of the saltation-abrasion model<sup>23</sup> with a stochastic  
68 model for bedrock landsliding<sup>27</sup> and multi-component sediment transport on hillslopes and  
69 in rivers<sup>28</sup>. We apply the saltation-abrasion formalism to model fluvial incision because of  
70 its solid foundation in physical principles based on experiments<sup>5,23</sup>. Bedrock landsliding is  
71 incorporated because threshold-hillslope processes, such as landsliding, play a dominant  
72 role in limiting relief in tectonically active regions<sup>9,11,20,21</sup> and because landslide magnitude  
73 and frequency are critical for providing abrasive agents to the fluvial system<sup>10,11,16,17,29</sup>.  
74 Landslides are important for scaling the erosion budget of tectonically active mountain  
75 ranges, which is most evident in the distinct threshold landscapes presently found for  
76 example in Taiwan<sup>29</sup> and Himalaya<sup>20,21</sup>. In addition to fluvial incision and bedrock  
77 landsliding, our computational experiments include slope-independent hillslope  
78 weathering, non-linear hillslope sediment transport, and grain-size dependent sediment  
79 transport in rivers (Methods).

80

81 The computational experiments are designed to primarily investigate the coupled impact of  
82 1) bedrock landsliding controlled by threshold slopes and 2) fluvial erosion driven by  
83 saltation-abrasion in rivers. We note that lithological contrasts not addressed by our model  
84 experiments also influence river incision rates, and, depending on the geological setting, the  
85 rock hardness may increase when long-term erosion exposes the deep and resistant core of  
86 mountain belts. Furthermore, additional erosion processes in rivers and on hillslopes may  
87 be of relevance in natural systems. The feedbacks between landslides and river incision that

88 we address here are likely to dominate in settings where sediment impacts drive bedrock  
89 abrasion and/or help produce joint blocks, while their significance will be less important in  
90 settings where chemical weathering plays the dominant role<sup>1</sup>. The aim here, however, is to  
91 demonstrate the fundamental impact of feedbacks between landslides and saltation-  
92 abrasion on fluvial incision rates in the context provided by the necessity to reconcile rapid  
93 incision rates in tectonically-active orogens, with the long-term survival of orogenic relief  
94 once tectonic activity ceases. To do so, we model a cross-section through an asymmetric  
95 mountain range generated by tectonic rock uplift in the shape of a two-sided wedge system  
96 (Fig 1). We focus on the influence of tectonic uplift on river erosion rates, and the results  
97 are independent of bedrock lithology as long as saltation-abrasion remains the dominant  
98 driver of river erosion. The spatially variable uplift rate allows us to study the influence of  
99 uplift rate on the resulting relief (supplementary Fig. S2). In order to demonstrate the key  
100 feedbacks, we have performed experiments with both the stream-power model and the  
101 saltation-abrasion model using the same coupling to bedrock landsliding and sediment  
102 transport (Methods).

103

104 Our results confirm that fluvial incision by saltation-abrasion generates landscape  
105 morphologies very similar to those predicted by stream-power models and observed in  
106 fluvial systems<sup>30</sup>. Channel profiles are upwards concave and drainage following the steepest  
107 topographic descent paths leads naturally to a system defined by catchments with large and  
108 gently dipping valleys and a number of steeper tributaries (Fig. 1). During the tectonically  
109 active phase, both the saltation-abrasion model and the stream-power model reach a  
110 topographic steady state where tectonic rock uplift is balanced by erosion everywhere in

111 the modelled landscape. Both models are associated with poorly constrained rate-limiting  
112 parameters (Methods), which we calibrate to obtain steady-state landscapes of similar  
113 mean (~1100 m) and maximum (~3500 m) elevation. The scale of this steady-state  
114 configuration resembles those of relatively small orogens like for example Taiwan or the  
115 Southern Alps. In the steady state configuration, bedrock landsliding represents a primary  
116 erosion mechanism in both models because hillslopes are allowed to reach threshold slopes  
117 in many places (supplementary discussion and supplementary Figs. S2 and S3).

118

119 While the steady-state topographic patterns are largely similar for the two models, the  
120 temporal variations in erosion rate differ significantly. The saltation-abrasion model reveals  
121 a highly dynamic system with several feedbacks (Figs. 2 and 3, supplementary Movie S1).  
122 When the landslide frequency increases, rivers receive more sediment and accelerate  
123 fluvial incision while the landslide detritus is moved through the drainage network (Fig. 2).  
124 This further accelerates the landslide frequency because hillslopes steepen as the base level  
125 set by the channel elevation is lowered. This positive feedback terminates when excessive  
126 sediment supply armours the riverbed. At this point, fluvial incision slows, reducing the  
127 likelihood of landslides, and a negative feedback between fluvial erosion and landslides is  
128 established that helps to temporarily stabilize the relief (Fig. 2). The pattern of highly  
129 oscillatory erosion flux changes when tectonic activity ceases. Then, continued rock uplift is  
130 due only to flexural-isostatic unloading, and the mean elevation of the landscape starts to  
131 decline. As hillslope gradients decrease below the critical threshold value for landsliding  
132 (Methods), the landslide frequency drops dramatically (Fig. 3A). The landslide frequency  
133 decreases in our models because tectonic rock uplift no longer maintains the steep

134 threshold slopes. The drop in landslide frequency may be even more dramatic in natural  
135 setting because earthquakes related to tectonic activity are viewed as important landslide  
136 triggers<sup>11</sup>. In the saltation-abrasion model, the decrease in landslide frequency leads to a  
137 corresponding decrease in the rate of fluvial incision, because of the associated decline in  
138 sediment input to the streams. The slowing fluvial erosion keeps channel elevations high,  
139 and this further reduces the landslide frequency. This is in stark contrast to the behaviour  
140 of the stream-power model (Fig. 3B), which exhibits a much more gradual decrease in  
141 erosion rate after tectonic uplift ceases because the stream-power erosion rate is scaled  
142 only by the local channel slope and water discharge. For a total discharge that is constant  
143 through time, the available stream power only decreases slowly as a consequence of the  
144 continued lowering of the landscape.

145

146 A sudden drop in landslide frequency and saltation-abrasion erosion has a significant effect  
147 on the post-orogenic lifespan. Our scaled model results show that peaks can stand above an  
148 elevation of 2 km for more than 200 Myr following the cessation of tectonic activity (Fig  
149 3C). That contrasts with our scaled stream-power model in which elevations above 2 km  
150 last only 20 Myr, because the stream-power erosion rates remain high in the absence of  
151 tectonic activity as long as significant relief persists. Both model experiments eventually  
152 terminate in similar transport-limited landscapes with main valleys that become  
153 permanently alluviated when the available stream-power decreases below the threshold  
154 required for sediment transport<sup>3,28</sup>. At this stage, the two models converge, but the duration  
155 of the transition to a transport-limited stage differs by more than an order of magnitude  
156 because the mechanisms dictating the rate of post-orogenic river incision in the two models

157 are fundamentally different. Landscapes in the stream-power model reach the transport-  
158 limited stage after only 25 Myr, whereas this transition takes more than ten times longer in  
159 the saltation-abrasion model. (Fig. 3C, supplementary discussion, supplementary Fig. S4).  
160 These precise figures depend on the details of the parameterization, but the order-of-  
161 magnitude difference in post-orogenic topographical lifespan stands as a robust result of  
162 the different fluvial erosion mechanisms. The prolonged lifespan of topography in the  
163 saltation-abrasion model is caused by the reduced influx of sediment to the rivers when  
164 tectonic activity stops, and we note that variations in bedrock exposure estimates<sup>6-8</sup> do not  
165 influence this result (supplementary Fig. S6). The interplay between hillslope processes and  
166 fluvial erosion by saltation-abrasion therefore provides a plausible physical mechanism for  
167 the presence of persistent, several hundred million years old, orogenic reliefs in tectonically  
168 inactive regions. The coupling of experimentally validated models, which incorporate the  
169 actual physics of the processes operating on hillslopes and in rivers, represents a new  
170 approach that is necessary to improve our understanding of the mechanisms that control  
171 the long-term evolution of mountain ranges.

172

### 173 **Method summary**

174 The landscape evolution model employed in this study computes the transport of water and  
175 sediment across a plan-form grid consisting of irregularly distributed Voronoi cells.  
176 Connecting neighbouring cells in the direction of steepest descent generates the fluvial  
177 surface transport network. Topographical depressions, which may for example arise from

178 dams generated by landslides, are filled by water that form lakes and ensure continuous  
179 drainage from every grid cell to the model boundaries.

180 The rate of fluvial incision into bedrock is calculated from either the saltation-abrasion  
181 model or the stream-power model. For computing saltation-abrasion, we include the full  
182 physics of the model presented by Sklar & Dietrich<sup>23</sup>. Both types of fluvial-erosion-models  
183 are coupled to models for bedrock landsliding<sup>27</sup>, sediment transport in rivers<sup>28</sup> and on  
184 hillslopes, long-term hillslope weathering<sup>27</sup>, and flexural isostasy. The various erosion  
185 components are coupled through their effects on bedrock topography and their  
186 contributions to a layer of transportable sediment. The fluvial sediment transport model  
187 operates with sediment of varying grain sizes in order to incorporate the effects of  
188 downstream fining on sediment transport capacity<sup>28</sup> and saltation-abrasion erosion rate<sup>23</sup>.  
189 The hillslope sediment transport model is independent of grain size, but includes non-linear  
190 effects of slope. We refer to the Extended Methods section and the supplementary  
191 information for more details on all model components.

192

### 193 **References**

- 194 1. F. von Blankenburg. The control mechanisms of erosion and weathering at basin  
195 scale from cosmogenic nuclides in river sediment. *Earth Planet. Sci. Lett.* **237**, 462-  
196 479 (2005).
- 197 2. P. Molnar, R. S. Andersen, S. P. Anderson. Tectonics, fracturing of rock, and erosion.  
198 *Jour. Geophys. Res.* **112**, F03014 (2007).

- 199        3. J. A. Baldwin, K. X. Whipple, G. E. Tucker. Implications of the shear stress river  
200              incision model for the timescale of postorogenic decay of topography. *Jour. of*  
201              *Geophys. Res.* **108**, 2158 (2003).
- 202        4. K. X. Whipple, G. S. Hancock, R. S. Anderson. River incision into bedrock: Mechanics  
203              and relative efficacy of plucking, abrasion, and cavitation. *GSA Bulletin* **112**, p. 490-  
204              503 (2000).
- 205        5. L. S. Sklar, W. E. Dietrich. Sediment and rock strength controls on river incision into  
206              bedrock. *Geology* **29**, 1087-1090 (2001).
- 207        6. G. S. Hancock, R. S. Anderson. Numerical modelling of fluvial strath-terrace formation  
208              in response to oscillating climate. *GSA Bulletin* **114**, p. 1131-1142 (2002).
- 209        7. J. M. Turowski, D. Lague, N. Hovius. Cover effects in bedrock abrasion: A new  
210              derivation and its implications for the modelling of bedrock channel morphology.  
211              *Jour. of Geophys. Res.* **112**, F04006 (2007).
- 212        8. B. J. Yanites et al. The influence of sediment cover variability on long-term river  
213              incision rates: An example from Peikang River, central Taiwan. *Jour. of Geophys. Res.*  
214              **116**, F03016 (2011).
- 215        9. I. J. Larsen, D. R. Montgomery. Landslide erosion coupled to tectonics and river  
216              incision. *Nature Geoscience* **5**, 468-473 (2012).
- 217        10. W. B. Ouimet et al. The influence of large landslides on river incision in a transient  
218              landscape: Eastern margin of the Tibetan Plateau (Sichuan, China). *GSA Bulletin* **119**,  
219              1462-1476 (2007).
- 220        11. O. Korup, A. L. Densmore, F. Schlunegger. The role of landslides in mountain range  
221              evolution. *Geomorphology* **120**, 77-90 (2010).

- 222        12. M. A. Seidl, W. E. Dietrich. The problem of channel erosion into bedrock. *Catena Suppl.* **23**, 101-124 (1992).
- 223
- 224        13. A. D. Howard, G. Kerby. Channel changes in badlands. *Geol. Soc. Am. Bull.* **94**, 739-752 (1983).
- 225
- 226        14. K. X. Whipple *et al.* Geomorphic limits to climate-induced increases in topographic relief. *Nature* **401**, 39-43 (1999).
- 227
- 228        15. E. Kirby, K. X. Whipple. Quantifying differential rock-uplift rates via stream profile analysis. *Geology* **29**, 415-418 (2001).
- 229
- 230        16. S. J. Dadson *et al.* Links between erosion, runoff variability and seismicity in the Taiwan orogen. *Nature* **426**, 648-651 (2003).
- 231
- 232        17. J. D. Stock *et al.* Field measurements of incision rates following bedrock exposure: Implications for process controls on the long profiles of valleys cut by rivers and debris flow. *Geol. Soc. Am. Bull.* **117**, 174-194 (2005).
- 233
- 234
- 235        18. C. S. Riebe *et al.* Minimal climatic control on erosion rates in the Sierra Nevada, California. *Geology* **29**, 447-450 (2001).
- 236
- 237        19. D. W. Burbank *et al.* Decoupling of erosion and precipitation in the Himalayas. *Nature* **426**, 652-655 (2003).
- 238
- 239        20. D. W. Burbank *et al.* Bedrock incision, rock uplift and threshold hillslopes in the northwestern Himalayas. *Nature* **379**, 505-510 (1996).
- 240
- 241        21. D. R. Montgomery, M. T. Brandon. Topographic controls on erosion rates in tectonically active mountain ranges. *Earth Planet. Sci. Lett.* **201**, 481-489 (2002).
- 242

- 243        22. F. von Blankenburg, T. Hewawasam, P. W. Kubik. Cosmogenic nuclide evidence for  
244                  low weathering and denudation in the wet, tropical highlands of Sri Lanka. *Jour. of*  
245                  *Geophys. Res.* **109**, F03008 (2004).
- 246        23. L. S. Sklar, W. E. Dietrich. A mechanistic model for river incision into bedrock by  
247                  saltating bed load. *Water Resour. Res.* **40**, W06301 (2004).
- 248        24. P. A. Cowie *et al.* New constraints on sediment-flux-dependent river incision:  
249                  Implications for extracting tectonic signals from river profiles. *Geology* **36**, 535-538  
250                  (2008).
- 251        25. K. X. Whipple, G. E. Tucker. Implications of sediment-flux-dependent river incision  
252                  models for landscape evolution. *J. Geophys. Res.* **107**, 2039 (2002).
- 253        26. N. M. Gasparini, K. X. Whipple, R. L. Bras. Predictions of steady state and transient  
254                  landscape morphology using sediment-flux-dependent river incision models. *J.*  
255                  *Geophys. Res.* **112**, F03S09 (2007).
- 256        27. A. L. Densmore, M. A. Ellis, R. S. Anderson. Landsliding and the evolution of normal-  
257                  fault-bounded mountains. *J. Geophys. Res.* **103**, 15203-15219 (1998).
- 258        28. P. R. Wilcock. Two-fraction model of initial sediment motion in gravel-bed rivers.  
259                  *Science* **280**, 410-412 (1998).
- 260        29. N. Hovius, C. P. Stark, C. Hao-Tsu, L. Jiun-Chuan. Supply and removal of sediment in a  
261                  landslide-dominated mountain belt: Central Range, Taiwan. *The Journal of Geology*  
262                  **108**, 73-89 (2000).
- 263        30. L. S. Sklar, W. E. Dietrich. Implications of the saltation-abrasion bedrock incision  
264                  model for steady-state river longitudinal profile relief and concavity. *Earth Surf.  
265                  Process. Landforms* **33**, 1129-1151 (2008).

266 **Author contributions**

267 DLE developed the computational modelling scheme and performed the modelling. All  
268 authors contributed equally to the design of the study and the writing of the paper.

269

270 **Figure legends**

271 **Fig 1.** The stream-power model and the saltation-abrasion model result in almost identical  
272 landscape morphologies when an asymmetrical wedge is uplifted and exposed to erosion.  
273 a) Minimum, mean, and maximum elevations along an east-west transects of the stream-  
274 power model. The red curve shows the variation in uplift rate, which peaks at  $1 \text{ mm yr}^{-1}$ . b)  
275 Detailed view of the resulting model landscape when bedrock landsliding is coupled to  
276 stream-power erosion. c) and d) show the same details for the saltation-abrasion model.  
277 The two models have similar drainage patterns because they evolve from the same initial  
278 condition defined by the same white-noise topography with an amplitude of 20 m.  
279 Threshold slopes (with ~35 degree hillslope angles) are more widely distributed in the  
280 model driven by saltation-abrasion, because the incision rate of this model may decrease  
281 when the channel slope increases beyond a critical value (supplementary Figs. S2 and S3).  
282 The full model geometry is shown in the supplementary Fig. S4.

283

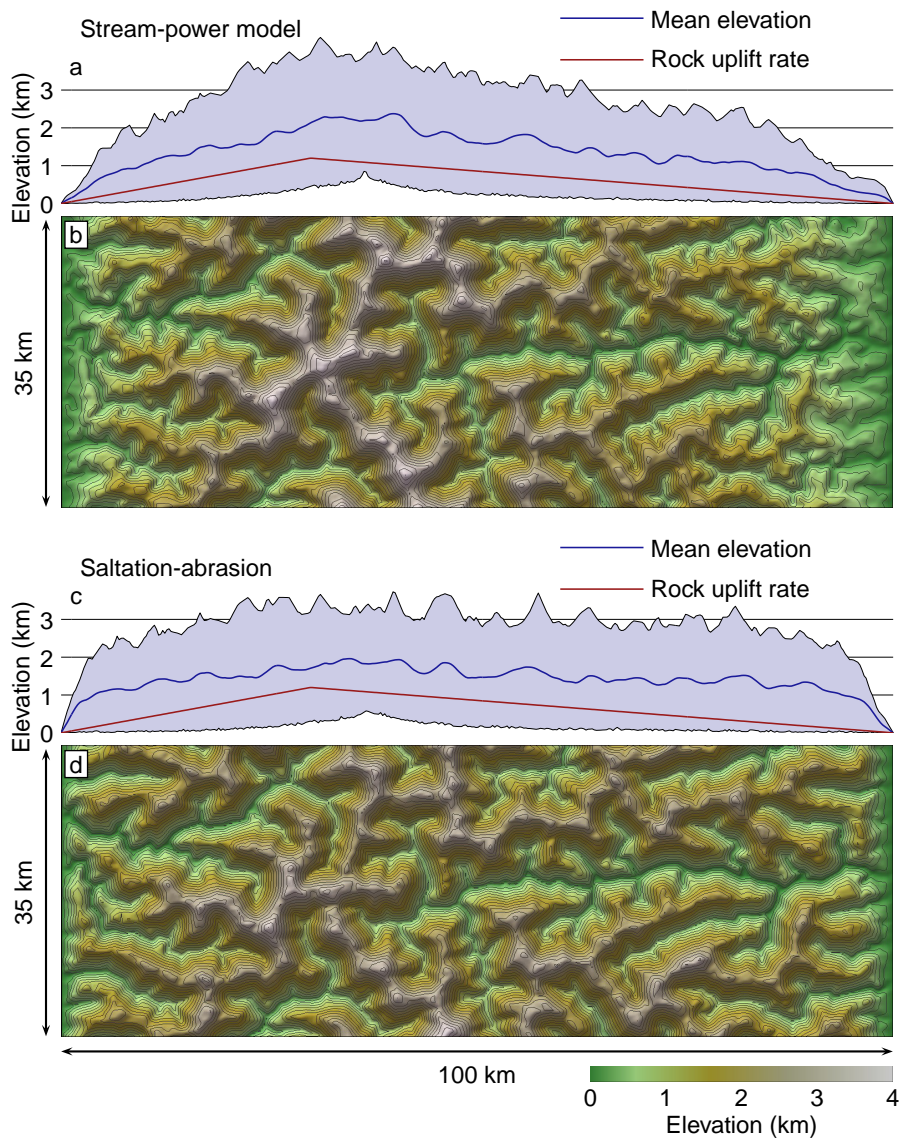
284 **Fig. 2.** Feedbacks between landsliding, fluvial incision, and sediment transport. a) The  
285 location of large landslides in one of the model's major catchment during a 100 kyr period  
286 with tectonic uplift. The circles indicate the location of the landslide initiation point. The  
287 size of the circles is scaled by landslide volume (red is  $> 0.3 \text{ km}^3$ , green  $> 0.2 \text{ km}^3$ , and gray  $>$

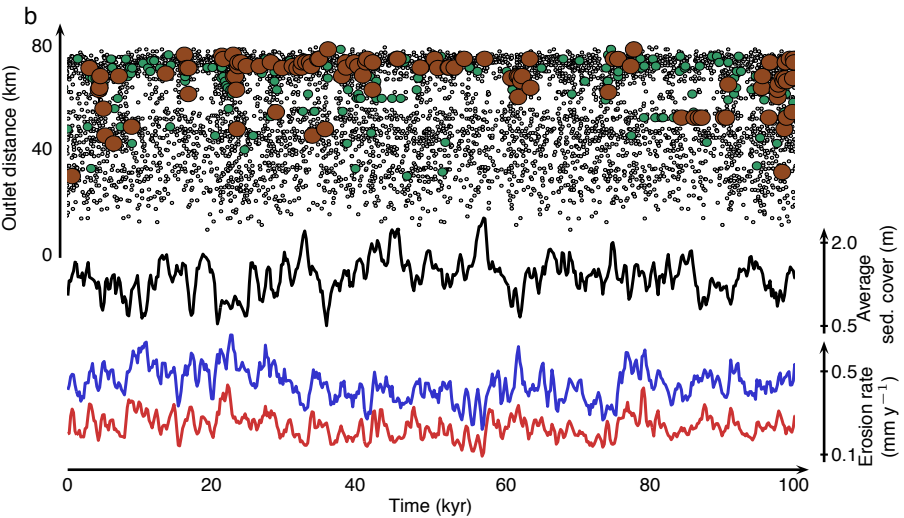
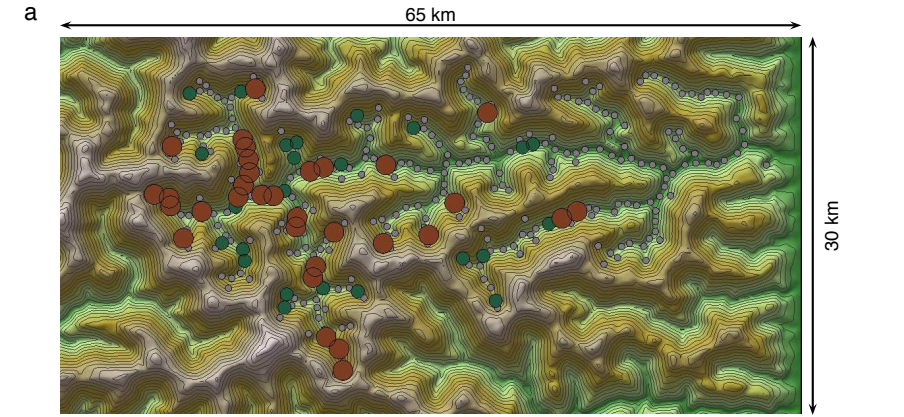
288 0.05 km<sup>3</sup>). The maximum elevation within the catchment is 3700 m. The contour spacing is  
289 200 m. The largest landslides are located near the model divide because this is the location  
290 of the highest uplift rates. b) The temporal distribution of landslides (colored circles) with  
291 distance to catchment outlet along the vertical axis. The figure also shows catchment  
292 averaged fluvial (red curve) and landslide (blue curve) erosion rates along with the  
293 averaged sediment thickness in the catchment (black curve). It is noticed that sediments  
294 accumulate in the catchment when many landslides occur almost simultaneously, which  
295 lowers the incision rate and thereby also the landslide frequency. When the sediment is  
296 again transported away from the catchment, fluvial incision rate and landslide frequency  
297 jointly rise. In supplementary Fig. S5, we show that the overall landslide frequency-size  
298 distribution conforms to a power-law distribution, although the occurrence of small  
299 landslides is limited by the resolution of the numerical model. Of greater importance is,  
300 however, the bulk landslide erosion rate (blue curve) representing the bulk sediment flux  
301 from the hillslopes to the river network.

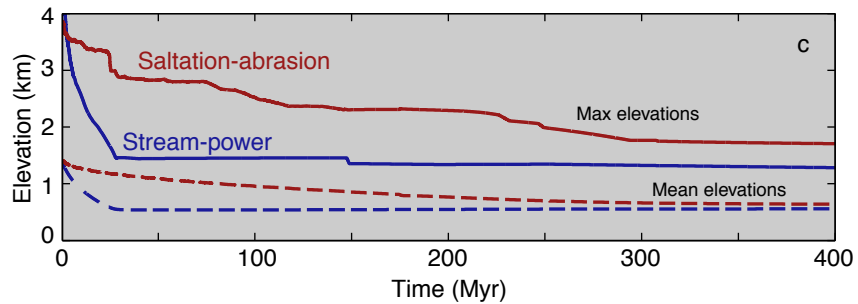
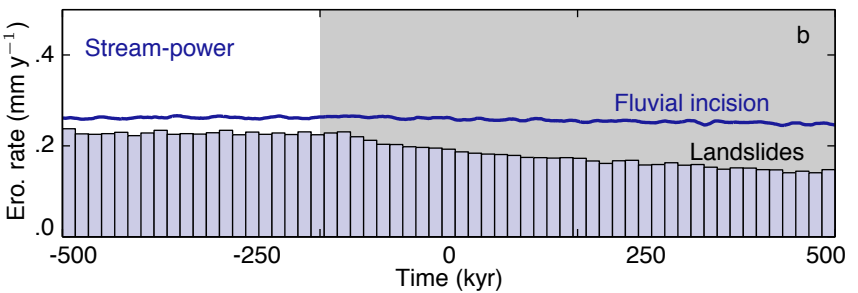
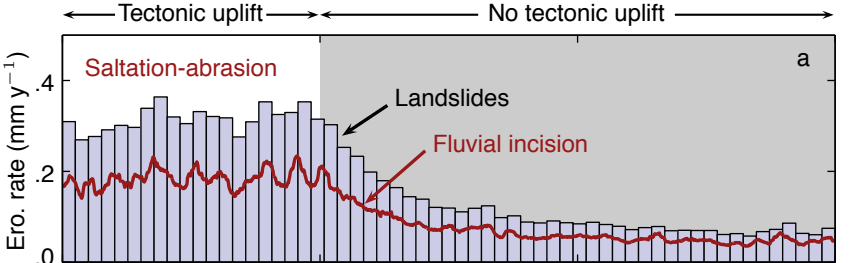
302

303 **Fig. 3.** While the erosion *patterns* are largely similar for the saltation-abrasion and stream-  
304 power models, the implications for erosion *rates* differs significantly for the two models. A  
305 highly dynamic system with several feedbacks emerges from the combination of saltation-  
306 abrasion and bedrock landsliding. a) Highly undulating erosion rates by saltation-abrasion  
307 and landsliding during the phase of tectonic uplift and slow erosion when tectonic activity  
308 stops. b) The combination of stream-power erosion and landslides does not include these  
309 feedbacks and erosion rates are not directly affected by tectonic activity. The grey bars in a)  
310 and b) represent landslide erosion rates averaged over 10 kyr intervals. c) Results of model

311 experiments covering 400 Myr of post-orogenic topographic evolution. The landscape of  
312 the saltation-abrasion model stays high for several hundred million years whereafter a  
313 steady transport-limited configuration is reached. The stream-power model achieves this  
314 configuration after only 25 Myr.







315 **Methods**

316

317 **River dynamics.** We modelled fluvial erosion and sediment transport across a two-dimensional  
 318 planform grid consisting of irregularly distributed Voronoi cells. The river pathways were es-  
 319 tablished by connecting neighboring cells in the direction of steepest descent in every time step  
 320 following the CASCADE algorithm<sup>31</sup>. The precipitation rate,  $p_r$ , was uniform across the grid, im-  
 321 plying that the volumetric water flux was  $Q_w = p_r A$ , where  $A$  is upstream catchment area.

322 We followed Tucker & Slingerland<sup>32</sup> in calculating the average bed shear stress as  $\tau_b = \rho_w(gQ_wS)^{\frac{2}{3}}W^{-\frac{2}{3}}$ ,  
 323 where  $\rho_w$  is the density of water;  $g$  is the acceleration due to gravity;  $S$  is channel slope. The chan-  
 324 nel width,  $W = k_w Q_w^{\frac{1}{2}}$ , is a function of surface water discharge where  $k_w$  is a constant channel  
 325 width scaling factor<sup>32</sup> (we refer to supplementary Table S1 for values of all model parameters).

326 **Sediment transport.** The applied landscape evolution model transports sediments in rivers and  
 327 on hillslopes. The computational experiments therefore included a layer of mobile sediment of  
 328 thickness  $H_s$ . The thickness of this sediment layer was updated by solving the continuity equation  
 329 for volume conservation:

$$\frac{\partial H_s}{\partial t} = -\nabla \cdot (q_{sf} + q_{sh}) + \frac{\rho_r}{\rho_s} (\dot{E}_f + \dot{E}_l + \dot{E}_h) \quad (1)$$

330 where  $q_{sf}$  and  $q_{sh}$  are the sediment fluxes in rivers and on hillslopes respectively.  $\rho_r$  and  $\rho_s$  are  
 331 the densities of bedrock and sediment.  $\dot{E}_f$ ,  $\dot{E}_l$ , and  $\dot{E}_h$  are the bedrock erosion rates due to rivers,  
 332 landslides, and hillslope weathering respectively. These erosion mechanisms are described in sep-  
 333 arate sections below.

334 For the downstream sediment transport in rivers ( $q_{sf}$ ), the transport model operated with sediment  
 335 of varying grain sizes. This made it possible to incorporate the effects of downstream fining on  
 336 sediment transport and bedrock erosion by saltation-abrasion. The total sediment volume was  
 337 therefore binned according to grain size,  $D$ , from  $\psi = 0, 1, 2, \dots, 8$ , where  $\psi = \log_2(D/D_0)$  is  
 338 a logarithmic grain size distribution<sup>33</sup> (supplementary Table S2) and  $D_0 = 1$  mm is a reference  
 339 grain size. The sediments were then transported by the two-fraction model of Wilcock<sup>28</sup>, wherein  
 340 the different grain sizes are combined in two groups: mixed sand ( $D \leq 2$  mm) and mixed gravel  
 341 ( $D > 2$  mm). Carrying capacities for sand and gravel were calculated from the two-fraction model  
 342 and rivers were assumed to run at capacity if enough sediment was available (we refer to the sup-

<sup>343</sup> plementary information for more information on the fluvial sediment transport model).  
<sup>344</sup> For sediment transport on hillslopes, we used a non-linear flux model<sup>34,35</sup> relating volumetric sed-  
<sup>345</sup> iment flux,  $q_{sh}$ , to the bed gradient,  $\nabla b$ :

$$q_{sh} = -K_s \frac{\nabla b}{1 - (|\nabla b|/s_c)^2} \quad (2)$$

<sup>346</sup> where  $s_c$  is the critical slope and  $K_s$  is a constant (supplementary Table S1). In this model, sed-  
<sup>347</sup> iment transport is inefficient on flat surfaces and more efficient on steep slopes that approach the  
<sup>348</sup> critical value  $s_c$ .

<sup>349</sup> **River erosion by saltation-abrasion.** The saltation-abrasion erosion rate,  $\dot{E}_f^{sa}$ , is expressed as the  
<sup>350</sup> product of three terms in the theory presented by Sklar & Dietrich<sup>23</sup>:

$$\dot{E}_f^{sa} = V_i I_r F_e \quad (3)$$

<sup>351</sup> where  $V_i$  is the average volume of bedrock detached per particle impact;  $I_r$  is the rate of particle  
<sup>352</sup> impact per unit area, and  $F_e$  (the sediment cover factor) is the fraction of the river bed that is free  
<sup>353</sup> of sediment and therefore exposed to erosion.

<sup>354</sup> We followed the approach of Sklar & Dietrich<sup>23</sup> closely and subsequently approximated Eqn. (3)  
<sup>355</sup> above with:

$$\dot{E}_f^{sa} = K_{sa} \frac{q_{sf}^\psi}{W} F_e [\tau^*/\tau_c^* - 1]^{-0.52} [1 - (u^*/w_f)^2]^{1.5} \quad (4)$$

<sup>356</sup> where  $K_{sa}$  is a lumped scaling parameter (supplementary information and supplementary Table  
<sup>357</sup> S1);  $q_{sf}^\psi$  is the sediment flux of a particular grain size;  $\tau^*$  is the non-dimensional Shield's stress;  $\tau_c^*$   
<sup>358</sup> is the non-dimensional critical threshold shear stress for sediment entrainment;  $u^* = \sqrt{\tau_b/\rho_w}$  is  
<sup>359</sup> the shear velocity;  $w_f$  is the settling velocity of sediment grains. The sediment-free fraction of the  
<sup>360</sup> river bed,  $F_e$ , was assumed to vary linearly between two end-member cases: 1) when the river runs  
<sup>361</sup> at capacity and the bed is fully alluviated ( $V_t = \Delta t Q_t$ , where  $V_t$  is the volume of sediment available  
<sup>362</sup> for transport,  $Q_t$  is the sediment transport capacity of the river segment, and  $\Delta t$  is the length of  
<sup>363</sup> the time step), and 2) when the river receives no sediment that can form patches of alluvial cover  
<sup>364</sup> ( $V_t = 0$ ):

$$F_e = \begin{cases} 1 - V_t/(\Delta t Q_t) & \text{for } V_t < \Delta t Q_t \\ 0 & \text{else} \end{cases} \quad (5)$$

<sup>365</sup> Importantly, besides the sediment carried by the river,  $V_t$  includes sediment deposited on the river  
<sup>366</sup> bed, which ensures that sediment not in transport also influence the sediment cover factor. We  
<sup>367</sup> performed additional experiments with other types of  $F_e$  functions that demonstrate the robustness  
<sup>368</sup> of our conclusions in respect to variations in  $F_e$  (supplementary Fig. S6).

<sup>369</sup> Eqn. 4 depends on grain size, and we therefore computed the total erosion rate by summing the  
<sup>370</sup> contributions to the erosion rate associated with the individual sediment grain size bins (supple-  
<sup>371</sup> mentary Table S2). The values of  $q_s^\psi$ ,  $\tau^*$ ,  $\tau_c^*$ , and  $w_f$  were therefore calculated separately for each  
<sup>372</sup> sediment grain size (we refer to the supplementary information for details on the grain size depen-  
<sup>373</sup> dence and for the full derivation of Eqn. 4).

<sup>374</sup> **Stream-power erosion.** For the model experiments using steam-power erosion, the fluvial erosion  
<sup>375</sup> rate was calculated from:

$$\dot{E}_f^{sp} = K_{sp} F_e Q_w^m S^n \quad (6)$$

<sup>376</sup> where  $K_{sp}$  is a rate-limiting constant<sup>36</sup>;  $Q_w$  is the water discharge (volumetric flux);  $S$  is channel  
<sup>377</sup> slope;  $m$  and  $n$  are constants (Table S2). Note that we included in the stream-power model the  
<sup>378</sup> protecting effect of a sediment cover by incorporating  $F_e$  from the saltation-abrasion theory (Eqn.  
<sup>379</sup> 5). By including the same protecting effects of sediments in all experiments, we effectively isolated  
<sup>380</sup> the differences between the two incision models (saltation-abrasion and stream-power erosion).  
<sup>381</sup> For example, by incorporating  $F_e$  in both models, we made sure that transport thresholds affected  
<sup>382</sup> both model types similarly.

<sup>383</sup> **Bedrock landslides.** We used the model presented by Densmore *et al.*<sup>27</sup> for simulating bedrock  
<sup>384</sup> landslides. The model is stochastic in the sense that the probability of hillslope failure depends  
<sup>385</sup> on the Culmann slope stability criterion<sup>27</sup>. The Culmann criterion predicts the maximum stable  
<sup>386</sup> height of a hillslope,  $H_c$ , from the angle of internal friction,  $\phi$ , the hillslope cohesion,  $C$ , and the  
<sup>387</sup> hillslope angle,  $\beta$ :

$$H_c = \frac{4C}{\rho_s g} \frac{\sin(\beta) \cos(\phi)}{1 - \cos(\beta - \phi)} \quad (7)$$

<sup>388</sup> In every time step of the model run, a fixed number,  $N_c$ , of random cells were checked for lands-  
<sup>389</sup> liding. From each of these cells (target-cells), the maximum extent of a stable plane was mapped  
<sup>390</sup> by recursively collecting in a list the up-slope cells with elevations above the cone shaped plane  
<sup>391</sup> that dips with angle  $\phi$  and passes through the target-cell. The stable plane must be continuous,

meaning that only cells that neighbor a cell already on the list was added to the list.  
After the list was generated, the hillslope height,  $H$ , and the hillslope angle,  $\beta$ , were established from the maximum elevation difference between the target-cell and cells on the list. The failure probability was computed from:

$$p_{\text{fail}} = \frac{H}{H_c} \quad (8)$$

The hillslope fails if a randomly generated number between 0 and 1 falls below  $p_{\text{fail}}$ .  
If failure occurred, the angle of the failure plane<sup>27</sup> was calculated from

$$\theta = \frac{1}{2} (\beta + \phi) \quad (9)$$

The failure plane was mapped by repeating the recursive procedure, now listing the cells with elevations above the cone-shaped failure plane dipping at angle  $\theta$ . The rock mass above the failure plane was eroded and passed to the target cell as new sediment.  
We assumed that the sediment generated in a landslide has a fractal distribution of grain sizes<sup>37</sup>:

$$N_\psi \propto D_\psi^{-f} \quad (10)$$

where  $N_\psi$  is the number of particles with diameters greater than  $D_\psi$  (Table S2).  $f = 2.65$  is the fractal dimension<sup>38</sup>.  
The fractal distribution was used to constrain the volume distribution of grain sizes within a landslide deposit:

$$V_s(\psi) = w_\psi V_{\text{landslide}} \quad (11)$$

where  $V_{\text{landslide}}$  is the total sediment volume generated by the landslide and  $w_\psi$  are volume weight functions associated with each grain size bin (supplementary Table S2). We note that the volume weights,  $w_\psi$ , was calculated to satisfy Eqn. 10.

**Hillslope weathering.** We followed Densmore *et al.*<sup>27</sup> by including non-linear sediment (regolith) production to simulate slow hillslope erosion on bare bedrock surfaces<sup>39</sup> (where  $H_s = 0$ ), faster erosion under moderate sediment thicknesses<sup>40</sup> ( $H_s \leq H_s^*$ ), and declining erosion rates under

<sup>412</sup> larger sediment thicknesses<sup>41</sup> ( $H_s > H_s^*$ ). In this model, the bedrock erosion rate is:

$$\dot{E}_h = \begin{cases} \dot{E}_0 + \frac{\dot{E}^* - \dot{E}_0}{H_s^*} H_s & \text{for } 0 \leq H_s \leq H_s^* \\ \dot{E}^* \exp\left(\frac{H_s^* - H_s}{\Delta H}\right) & \text{for } H_s > H_s^* \end{cases} \quad (12)$$

<sup>413</sup> All parameters are listed in supplementary Table S1.

<sup>414</sup> We assumed that the grain sizes of the sediments produced by weathering is of the same fractal  
<sup>415</sup> distribution as for landsliding (Eqn. 10), and the volume weights of Table S2 were therefore  
<sup>416</sup> reused. We note that grain sizes are likely to be smaller for sediments generated by weathering than  
<sup>417</sup> by landsliding. However, using the same gain sizes for both erosion processes is a conservative  
<sup>418</sup> assumption, because the saltation-abrasion erosion process puts a premium on the coarser fractions.  
<sup>419</sup> Reducing sediment grain sizes for weathering would therefore further slow saltation-abrasion rates  
<sup>420</sup> and amplify the difference between the saltation-abrasion and stream-power models.

<sup>421</sup> **Flexural isostasy.** Flexural isostatic adjustments,  $W_f(x, y)$ , in response to erosional unloading and  
<sup>422</sup> sediment deposition, were performed according to the two-dimensional elastic thin plate equation:

$$\frac{\partial^4 W_f}{\partial x^4} + 2 \frac{\partial^4 W_f}{\partial x^2 \partial y^2} + \frac{\partial^4 W_f}{\partial y^4} = \frac{L(x, y)}{D_f} \quad (13)$$

<sup>423</sup> Here  $D_f = YT_e^3/[12(1 - \nu^2)]$  is the flexural rigidity;  $Y$  is Young's modulus;  $\nu$  is the Poisson ratio,  
<sup>424</sup> and  $T_e$  is the elastic thickness of the lithosphere (supplementary Table S1).  $L(x, y) = \rho_r g E(x, y) -$   
<sup>425</sup>  $\rho_s g H_s(x, y) - \rho_a g W_f(x, y)$  is the vertical load on the plate (positive upward);  $E(x, y)$  is the total  
<sup>426</sup> bedrock erosion in each model cell;  $H_s(x, y)$  is the amount of sediment present;  $\rho_a$  is the density  
<sup>427</sup> of the isostatically compensating asthenosphere rocks.

- <sup>429</sup> 31. Braun, J. & Sambridge, M. Modelling landscape evolution on geological time scales: a new  
<sup>430</sup> method based on irregular spatial discretization. *Basin Research* **9**, 27–52 (1997).
- <sup>431</sup> 32. Tucker, G. E. & Slingerland, R. L. Predicting sediment flux from fold and thrust belts. *Basin*  
<sup>432</sup> *Research* **8**, 329–349 (1996).
- <sup>433</sup> 33. Parker, G. & Andrews, E. D. Sorting of bedload sediment by flow in meander bends. *Water*  
<sup>434</sup> *Resour. Res.* **21**, 1395–1408 (1985).

- 435 34. Andrews, D. J. & Bucknam, R. C. Fitting degradation of shoreline scarps by a nonlinear  
436 diffusion model. *Journal of Geophysical Research* **92**, 12857–12867 (1987).
- 437 35. Roering, J. J., Kirchner, J. W. & Dietrich, W. E. Evidence for nonlinear, diffusive sediment  
438 transport and implications for landscape morphology. *Water Resources Research* **35**, 853–870  
439 (1999).
- 440 36. Howard, A. D. A detachment-limited model of drainage basin evolution. *Water Resour. Res.*  
441 **30**, 2261–2285 (1994).
- 442 37. Turcotte, D. *Fractals and chaos in geology and geophysics* (Cambridge University Press,  
443 Cambridge, 1992).
- 444 38. Crosta, G., Frattini, P. & Fusi, N. Fragmentation in the Val Pola rock avalanche, Italian Alps.  
445 *Journal of Geophysical Research* **112**, F01006 (2007).
- 446 39. Small, E. E., Anderson, R. S. & Hancock, G. S. Estimates of the rate of regolith production  
447 using  $^{10}\text{Be}$  and  $^{26}\text{Al}$  from an alpine hillslope. *Geomorphology* **27**, 131–150 (1999).
- 448 40. Ahnert, F. Brief description of a comprehensive three-dimensional process-response model of  
449 landform development. *Z. Geomorphol.* **24**, 11–22 (1970).
- 450 41. Heimsath, A. M., Dietrich, W. E., Nishiizumi, K. & Finkel, R. C. The soil production function  
451 and landscape equilibrium. *Nature* **388**, 358–361 (1997).

## Supplementary information for:

### *Lifespan of mountain ranges scaled by feedbacks between landslides and erosion by rivers*

D. L. Egholm\*, M. F. Knudsen, M. A. Sandiford

\*To whom correspondance should be addressed: david@geo.au.dk

## Contents

<b>1</b>	<b>Supplementary figures</b>	<b>2</b>
Figure S1   Notable examples of old mountain ranges with high topographic relief . . . . .	2	
Figure S2   The steady-state surface slope distribution as function of rock uplift rate . . . . .	3	
Figure S3   Saltation-abrasion incision rates for various grain sizes as function of channel slope . . . . .	4	
Figure S4   Post-orogenic evolution of the model landscapes. . . . .	5	
Figure S5   Landslide magnitude and frequency . . . . .	6	
Figure S6   Post-orogenic life-span of saltation-abrasion models with other $F_e$ functions . . . . .	7	
<b>2</b>	<b>Supplementary tables</b>	<b>8</b>
Table S1   Parameter values for the computational model . . . . .	8	
Table S2   Sediment grain size bins . . . . .	9	
<b>3</b>	<b>Supplementary methods section</b>	<b>10</b>
3.1 Sediment transport in rivers . . . . .	10	
3.2 Erosion by saltation-abrasion . . . . .	11	
<b>4</b>	<b>Supplementary discussion section</b>	<b>13</b>
4.1 On the distribution of threshold slopes . . . . .	13	
<b>5</b>	<b>Caption for supplementary movie S1</b>	<b>14</b>

## 1 Supplementary figures

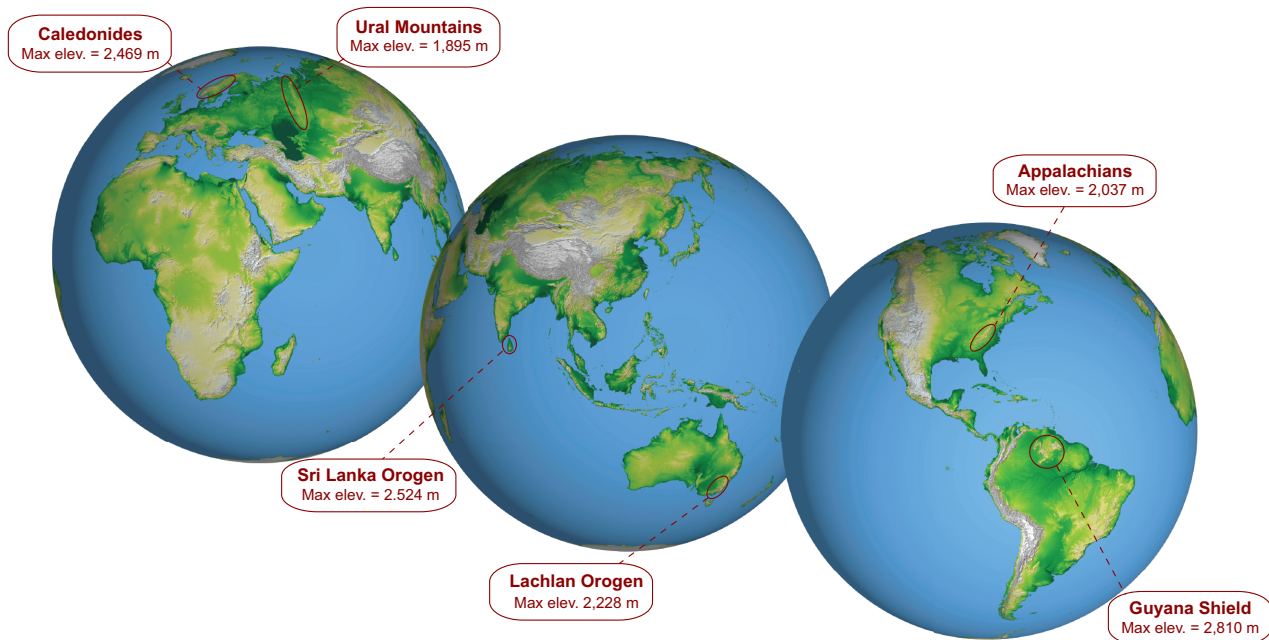


**Figure S1 | Notable examples of old mountain ranges with high topographic relief.** The delineated areas mark regions characterized by mountaneous topography, including high reliefs and steep slopes, that has been preserved over several hundred million years. Despite the high reliefs, and in some cases, high rainfall rates, these regions are all characterized by slow erosion rates. The presence of these orogenic reliefs represents a paradox as they should have eroded away long ago according to the existing models for fluvial erosion. The several hundred million-year old Sri Lanka Orogen highlights this paradox, because the high rainfall rate and high relief in this area should have accelerated erosion and lowered the topography as dictated by the stream-power concept.

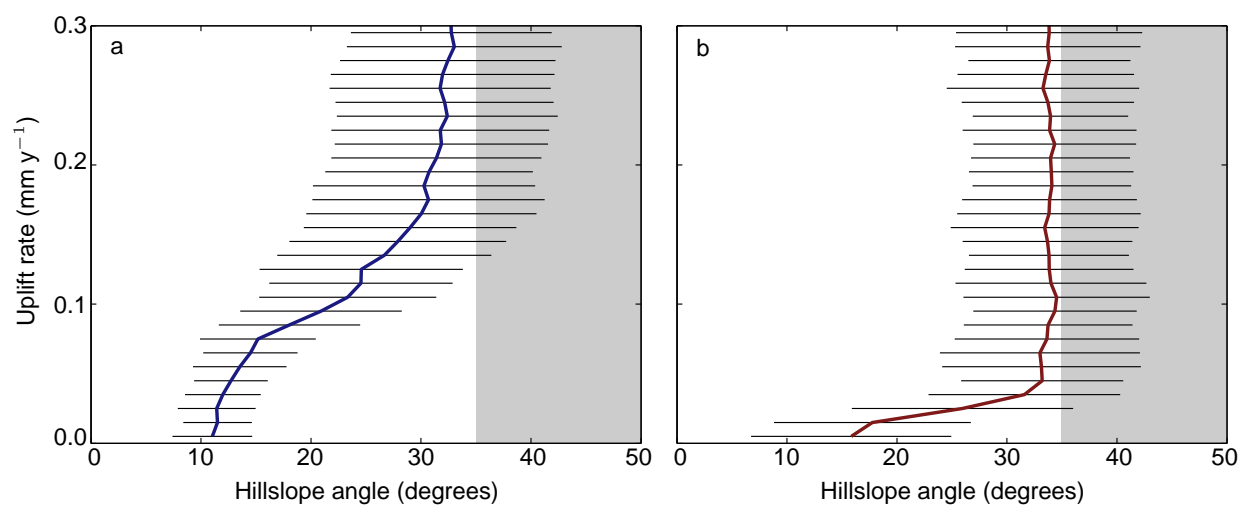


**Figure S2 | The steady-state surface slope distribution as function of rock uplift rate.** a) The stream-power model. b) The saltation-abrasion model. Solid curves represent mean slope values, while the black horizontal lines indicate the associated standard deviation. The grey area represents the domain of unstable bedrock slopes. Threshold slopes are widespread in both situations, but occur more often in the saltation-abrasion model because erosion-rate can decrease with increasing surface slope. This causes channel slopes to increase more rapidly towards landslide thresholds.

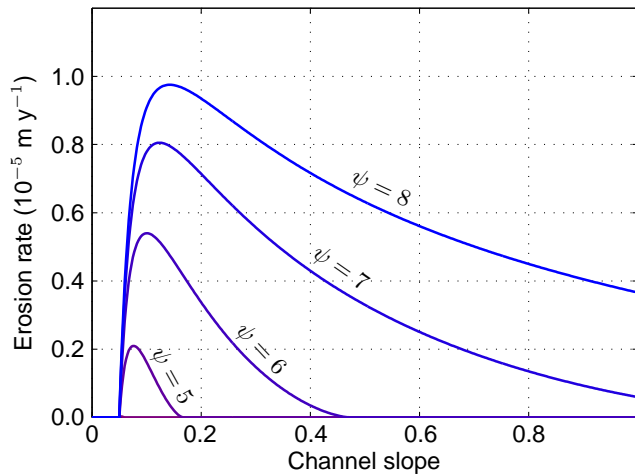


**Figure S3 | Saltation-abrasion incision rates for various grain sizes as function of channel slope.** The saltation-abrasion incision rate depends non-linearly on slope because the shear stress contributes to both impact velocity and hop length. For small slopes, the influence on impact velocity dominates the increasing hop length, and the erosion rate increases with slope. The influence on hop length becomes more important for larger slopes, and the erosion rate starts to decrease with increasing slope. Each curve represents a grain size bin,  $\psi$  (Table S2). We refer to Sklar & Dietrich<sup>1,2</sup> for more details on the slope dependence of the saltation-abrasion model.

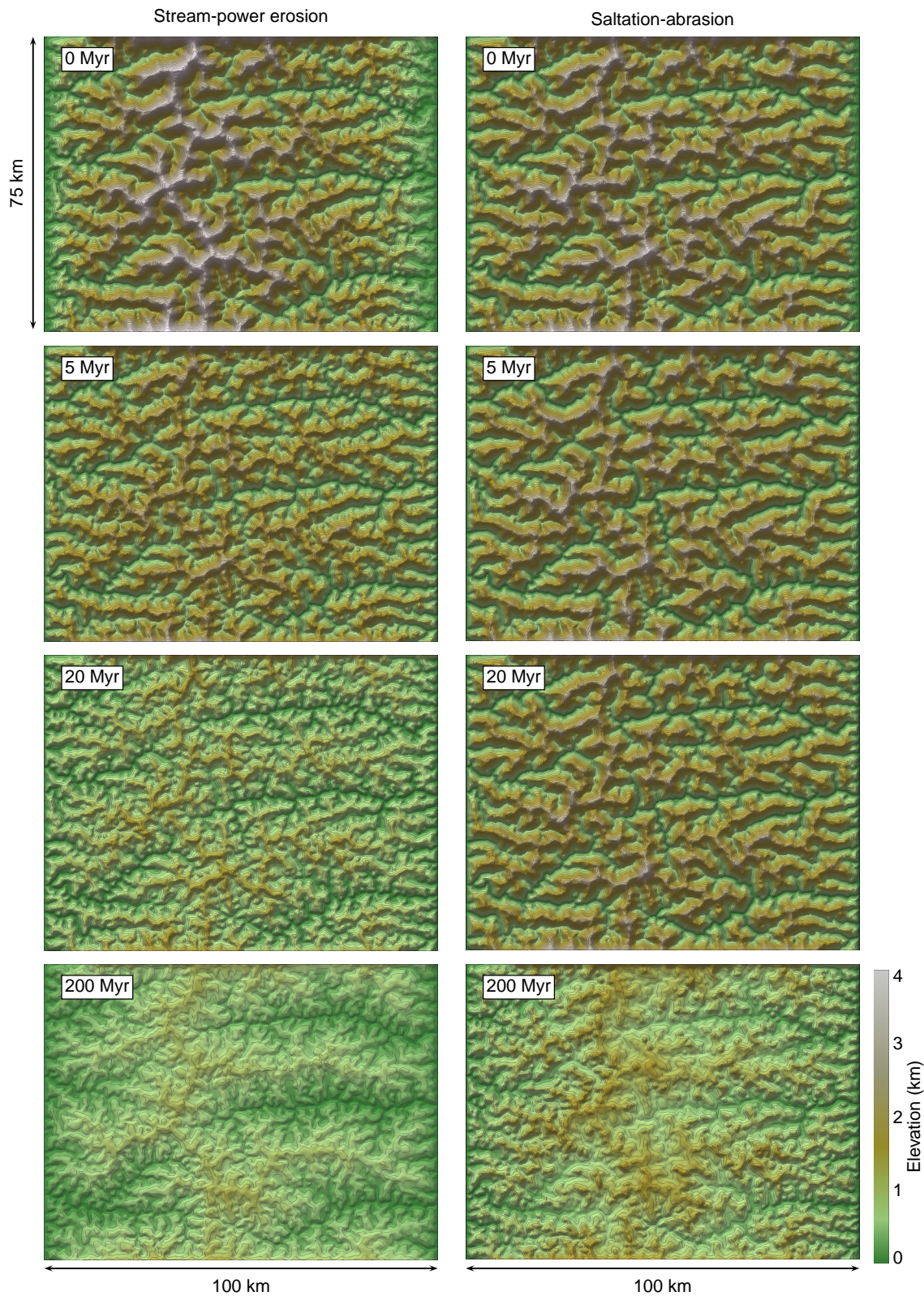


**Figure S4 | Post-orogenic evolution of landscapes controlled by stream-power erosion (left) and saltation-abrasion (right), respectively.** The two models in their tectonically active steady-state (0 Myr) and 5, 20, and 200 Myr after tectonic rock uplift has terminated. In this post-orogenic phase, rock uplift only occurs by flexural isostacy. The stream-power model reaches a sediment-transport threshold state after 25 Myr. The saltation-abrasion model requires 300 Myr to reach the same topographically subdued threshold configuration.

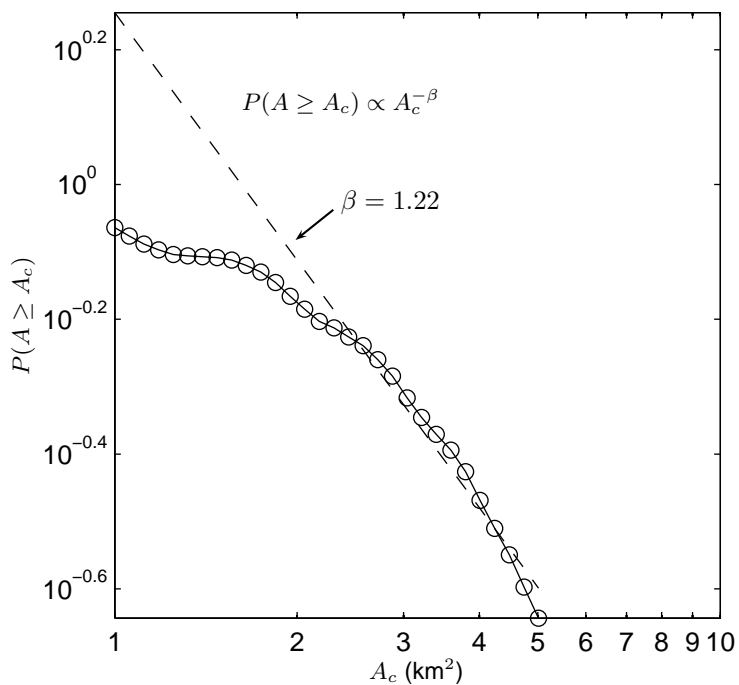


**Figure S5 | Landslide frequency and magnitude.** The landslide magnitude-frequency distribution of the computational experiments. The probability function  $P(A \geq A_c)$  is calculated as  $N(A \geq A_c)/N_t$  where  $A$  is landslide area;  $N(A \leq A_c)$  is the number of landslides of area greater than  $A_c$ ;  $N_t$  is the total number of recorded landslides. The distribution follows a power law for landslide areas greater than  $2 \text{ km}^2$ . The scale invariant power law relation agrees with observations from nature<sup>3,4</sup>. For landslides of area less than  $2 \text{ km}^2$ , the spatial resolution of the model limits the frequency of landslides.

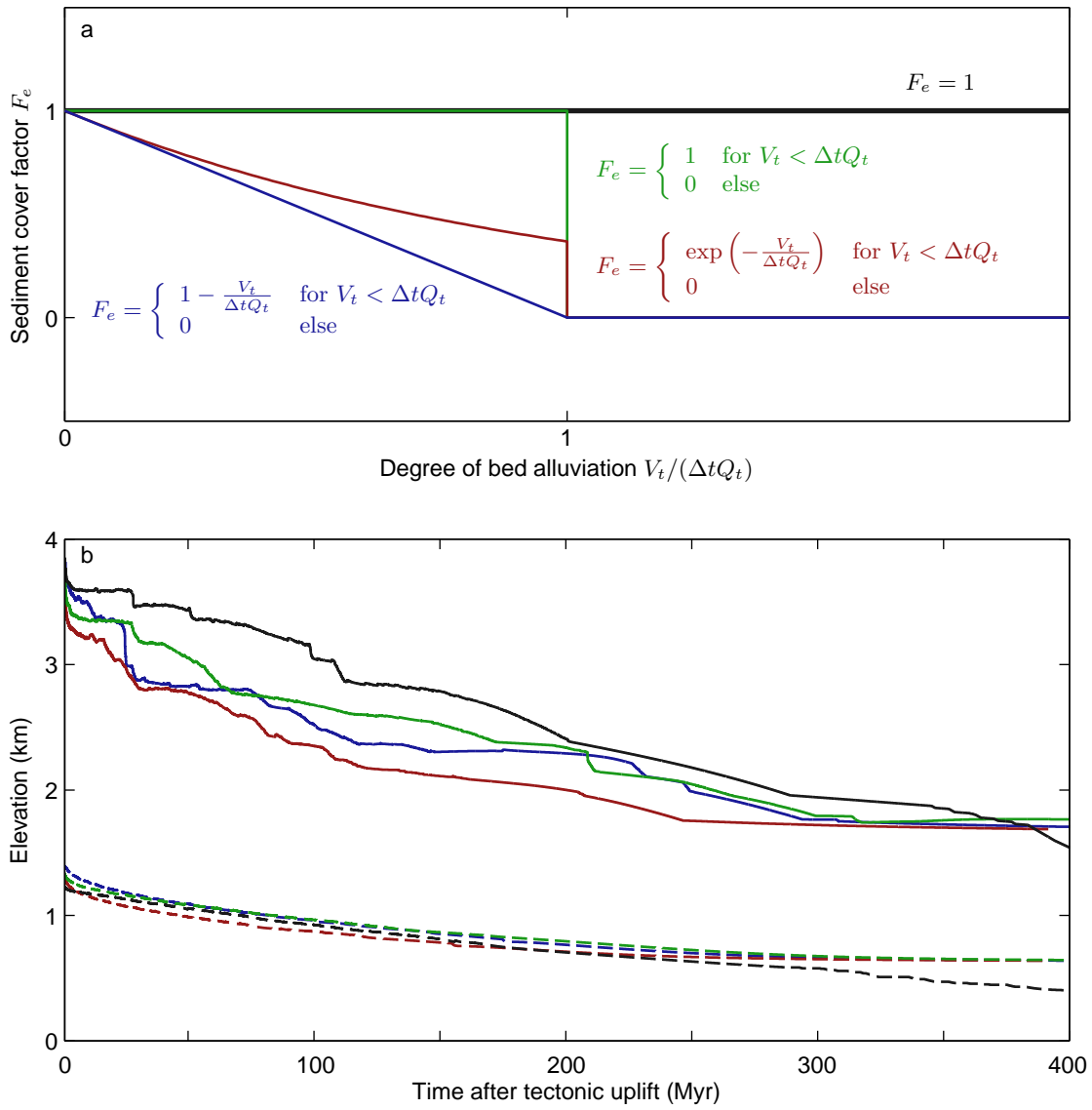


**Figure S6 | Post-orogenic life-span for saltation-abrasion models with various sediment cover factor functions.** In order to study the effect of the sediment cover factor for the post-orogenic evolution, we performed experiments with various  $F_e$  functions. a) The  $F_e$  functions.  $V_t$  is total sediment volume present in a grid cell, and  $\Delta t Q_t$  is the total volumetric transport capacity of the same cell. b) The evolution of maximum elevation (solid lines) and mean elevation (dashed lines) through time. The color of the lines corresponds to the colors in panel a. The black experiment (the black lines) is an end-member for which the sediment cover effect is always zero. The green experiment has a simple step function with no effect of sediment cover ( $F_e = 0$ ) when the sediment transport capacity exceeds the volume of sediment present, and full cover effect ( $F_e = 1$ ) when the river is overloaded with sediment. The red experiment has an exponential  $F_e$  function as suggested by Turowski et al.<sup>5</sup>, while the blue experiment represents the linear relation used in the present study. In order for the four different model experiments to deliver the same erosional efficiency in the steady-state phase with tectonic uplift (and therefore start the post-orogenic phase with similar max and mean elevation), the parameter  $K_f^{sa}$  was adjusted between experiments.  $K_f^{sa}$  was  $0.0003 \text{ m}^{-1}$  for the black experiment,  $0.00045 \text{ m}^{-1}$  for the green experiment,  $0.0008 \text{ m}^{-1}$  for the red experiment and  $0.0008 \text{ m}^{-1}$  for the blue experiment. We note that the variations in  $F_e$  relations does not affect the post-orogenic life-span of topography, because this is scaled mainly by the availability of abrasive tools, rather than the protective effect of a sediment cover.

## 2 Supplementary tables

Symbols	Descriptions	Values
$\rho_w$	Water density	1000 kg m <sup>-3</sup>
$\rho_s$	Sediment density	2300 kg m <sup>-3</sup>
$\rho_r$	Bedrock density	2700 kg m <sup>-3</sup>
$\rho_a$	Asthenosphere density	3200 kg m <sup>-3</sup>
$p_r$	Precipitation rate	2.0 m y <sup>-1</sup>
$k_w$	Channel width scaling factor	10 m <sup>-0.5</sup> s <sup>0.5</sup>
$g$	Acceleration due to gravity	9.82 m s <sup>-2</sup>
$Y$	Young's modulus of elasticity	10 <sup>11</sup> Pa
$D_0$	Reference grain size	1 mm
$D_s$	Sand median grain size	0.001 m
$D_g$	Gravel median grain size	0.1 m
$K_f^{sp}$	Erosion constant for stream power model	0.35 m <sup>-0.5</sup> yr <sup>-0.5</sup>
$K_f^{sa}$	Erosion constant for saltation abrasion model	0.0008 m <sup>-1</sup>
$m$	Stream power discharge exponent	0.5
$n$	Stream power slope exponent	1.0
$\phi$	Hillslope friction angle	35°
$C$	Hillslope cohesion	6000 kg m <sup>-1</sup> s <sup>-2</sup>
$N_c$	Number of random cells checked for landslides per time step	100
$\dot{E}_0$	Sediment production rate from bare rock	10 <sup>-5</sup> m y <sup>-1</sup>
$\dot{E}^*$	Maximum sediment production rate	5 × 10 <sup>-5</sup> m y <sup>-1</sup>
$H_s^*$	Depth of maximum sediment production rate	1.0 m
$\Delta H$	Decay length of sediment production rate	1.0 m
$K_s$	Hillslope sediment transport rate	0.01 m <sup>2</sup> y <sup>-1</sup>
$s_c$	Critical slope for sediment transport	20°
$T_e$	Lithosphere elastic thickness	10 km
$\nu$	Poisson ratio	0.25
$\Delta t$	Time step length	10 y

**Table S1** | Parameter values for the computational model

$\psi$	0	1	2	3	4	5	6	7	8
$D$ (mm)	1.00	2.00	4.00	8.00	16.0	32.0	64.0	128	256
$w_\psi$	0.033	0.043	0.054	0.069	0.088	0.112	0.143	0.182	0.276

**Table S2** | Sediment grain size bins,  $\psi$ , and the associated grain sizes,  $D = D_0 2^\psi$ , where  $D_0 = 1$  mm. The weights,  $w_\psi$ , are used for allocating new sediments to the bins. The weights are based on a fractal distribution.

### 3 Supplementary methods section

#### 3.1 Sediment transport in rivers

As described in the Methods section, we used Wilcock's two-fraction model<sup>6</sup> for transporting sediments of various grain sizes in rivers. For use in the saltation-abrasion theory, the total sediment volume was binned according to grain size,  $D$ , from  $\psi = 0, 1, 2, \dots, 8$ , where  $\psi = \log_2(D/D_0)$  is a logarithmic grain size distribution<sup>7</sup> (Table S2) and  $D_0 = 1$  mm is a reference grain size. However, in Wilcock's transport model, the sediment grain sizes are lumped into two groups: mixed sand ( $D \leq 2$  mm) and mixed gravel ( $D > 2$  mm). The proportions of gravel and sand on the bed are, respectively,  $f_g = V_g/V_t$  and  $f_s = V_s/V_t$ , where  $V_g$  and  $V_s$  are the volumes of gravel and sand.  $V_t = V_g + V_s$  is the total volume of sediment. According to Wilcock<sup>6</sup>, the transport equations for the two fractions are

$$Q_{tg} = 11.2 \frac{f_g W}{R_b g} \left( \frac{\tau_b}{\rho_w} \right)^{1.5} \left( 1.0 - 0.846 \frac{\tau_{gc}^*}{\tau_g^*} \right)^{4.5} \quad (1)$$

$$Q_{ts} = 11.2 \frac{f_s W}{R_b g} \left( \frac{\tau_b}{\rho_w} \right)^{1.5} \left( 1.0 - 0.846 \sqrt{\frac{\tau_{sc}^*}{\tau_s^*}} \right)^{4.5} \quad (2)$$

where  $Q_{tg}$  and  $Q_{ts}$  are the transport capacities (volumetric flux) of the gravel and sand components, respectively.  $R_b \equiv (\rho_r - \rho_w)/\rho_w$  and  $\rho_r$  is sediment grain density. The total volumetric carrying capacity of the river is  $Q_t = Q_{tg} + Q_{ts}$ . The actual flux of sediment,  $q_{sf}^\psi$ , belonging to a certain grain size bin,  $\psi$  (Table S2), is limited by the volume of that sediment,  $V_\psi$ , present in a cell:

$$q_{sf}^\psi = \begin{cases} \min \left( \frac{V_\psi}{V_s} Q_{ts}, \frac{V_\psi}{\Delta t} \right) & \text{for } 0 \leq \psi \leq 2 \\ \min \left( \frac{V_\psi}{V_g} Q_{tg}, \frac{V_\psi}{\Delta t} \right) & \text{for } 3 \leq \psi \leq 8 \end{cases} \quad (3)$$

The non-dimensional Shield's stress for gravel,  $\tau_g^*$ , and sand,  $\tau_s^*$ , are computed using the median grain sizes of gravel,  $D_g$ , and sand,  $D_s$ <sup>6</sup>:

$$\tau_g^* = \frac{\tau_b}{(\rho_r - \rho_w)gD_g} \quad (4)$$

$$\tau_s^* = \frac{\tau_b}{(\rho_r - \rho_w)gD_s} \quad (5)$$

In Eqns. (1) and (2),  $\tau_{gc}^*$  and  $\tau_{sc}^*$  are the non-dimensional critical threshold shear stresses for entrainment of gravel and sand, respectively (i.e. the values of  $\tau_g^*$  and  $\tau_s^*$  at the threshold of particle motion). Wilcock<sup>8</sup> demonstrated that  $\tau_{gc}^*$  and  $\tau_{sc}^*$  both depend on the sand proportion. In particular,  $\tau_{sc}^*$  is high in a gravel-rich bed (low  $f_s$ ) because the small amount of sand grains tends to 'hide' between the larger gravel particles. The sand is therefore protected from the stress of the river. In contrast, gravel on a sand-rich bed (high  $f_s$ ) is very exposed to the shear stress and  $\tau_{gc}^*$  therefore decreases with  $f_s$ . We follow Gasparini *et al.*<sup>9</sup> in using the following piecewise linear functions for satisfying the experimental data of Wilcock<sup>8</sup>:

$$\tau_{gc}^* = \begin{cases} 0.04 & \text{for } f_s \leq 0.1 \\ 0.04 - 0.1(f_s - 0.1) & \text{for } 0.1 < f_s \leq 0.4 \\ 0.01 & \text{else} \end{cases} \quad (6)$$

26 and

$$\tau_{sc}^* = \begin{cases} 0.88 & \text{for } f_s \leq 0.1 \\ 0.88 - 2.8(f_s - 0.1) & \text{for } 0.1 < f_s \leq 0.4 \\ 0.04 & \text{else} \end{cases} \quad (7)$$

### 27 3.2 Erosion by saltation-abrasion

28 We provide in the following section a full summary of Sklar & Dietrich's theory<sup>1</sup> for saltation-abrasion in  
 29 rivers. The section complements the details given in the Methods section.

30 The saltation-abrasion erosion rate,  $\dot{E}_f^{sa}$ , is expressed as the product of three terms in the theory presented  
 31 by Sklar & Dietrich<sup>1</sup>:

$$\dot{E}_f^{sa} = V_i I_r F_e \quad (8)$$

32 where  $V_i$  is the average volume of bedrock detached per particle impact;  $I_r$  is the rate of particle impact per  
 33 unit area, and  $F_e$  is the fraction of the river bed that is free of sediment and therefore exposed to erosion.

34 By treating bedrock as an elastic brittle material and adopting an established wear model<sup>10</sup>, Sklar & Diet-  
 35 rich<sup>1</sup> found that

$$V_i = \frac{\pi \rho_r D^3 w_{si}^2 Y}{6 k_v \sigma_T^2} \quad (9)$$

36 where  $Y$ ,  $k_v$ , and  $\sigma_T$  are brittle-elastic rock properties<sup>1</sup>;  $\rho_r$  and  $D$  are, respectively, sediment grain density and  
 37 grain size.

38 The vertical impact velocity,  $w_{si}$ , is the vertical component of the particle impact velocity with the bed.  $w_{si}$  is  
 39 assumed to be twice the mean descent velocity,  $w_{sd}$ <sup>1</sup>:

$$w_{si} \simeq 2w_{sd} = 3u_s \frac{H_s}{L_s} \quad (10)$$

40 where  $u_s$  is the mean downstream saltation velocity;  $H_s$  is the saltation hop height;  $L_s$  is the saltation hop  
 41 length.

42 The particle impact rate,  $I_r$ , is calculated as the flux of particles in transport per unit stream width divided  
 43 by the downstream distance between impacts. Assuming that the distance between impacts equals the particle  
 44 hop length,  $L_s$ , and calculating the particle flux as volumetric sediment flux of a particular grain size bin,  $q_{sf}^\psi$ ,  
 45 divided by the average particle volume gives

$$I_r = \frac{6q_{sf}^\psi}{\pi D(\psi)^3 W L_s} \quad (11)$$

46 The sediment-free fraction of the river bed is assumed to vary linearly between two end-member cases: 1)  
 47 when the river runs at capacity and the bed is fully alluviated ( $V_t = \Delta t Q_t$ ), and 2) when the river receives no  
 48 sediment that can form patches of alluvial cover ( $V_t = 0$ ):

$$F_e = \begin{cases} 1 - V_t / (\Delta t Q_t) & \text{for } V_t < \Delta t Q_t \\ 0 & \text{else} \end{cases} \quad (12)$$

49 Combining Eqns. 8-12 yields:

$$\dot{E}_f^{sa} = \frac{9\rho_r Y}{k_v \sigma_T^2} \frac{q_{sf}^\psi}{W} F_e \frac{u_s^2}{L_s} \frac{H_s^2}{L_s^2} \quad (13)$$

50 In order to relate the saltation velocity,  $u_s$ , the hop length,  $L_s$ , and the hop height,  $H_s$ , to shear stress,  $\tau^*$   
 51 and shear velocity  $u^* = \sqrt{\tau_b/\rho_w}$ , Sklar & Dietrich<sup>1</sup> constructed empirical expressions based on a large data set  
 52 from experimental saltation studies. By performing log-log linear data regression, Sklar & Dietrich<sup>1</sup> obtained  
 53 the following relations:

$$u_s = 1.56 (R_b g D)^{-0.5} \left[ \left( \frac{\tau^*}{\tau_c^*} \right) - 1 \right]^{0.56} \quad \text{for } \tau^*/\tau_c^* > 1 \quad (14)$$

$$\frac{L_s}{D} = 8.0 (\tau^*/\tau_c^* - 1)^{0.88} \left[ 1 - (u^*/w_f)^2 \right]^{-0.5} \quad \text{for } u^*/w_f < 1 \quad (15)$$

$$\frac{L_s}{H_s} = 5.6 (\tau^*/\tau_c^* - 1)^{0.38} \left[ 1 - (u^*/w_f)^2 \right]^{-0.5} \quad \text{for } u^*/w_f < 1 \quad (16)$$

54 The particle settling velocity in still water,  $w_f$ , is approximated by the general square-root relation from  
 55 Rubey<sup>11</sup>:

$$w_f = \sqrt{\frac{4}{3} g R_b D} \quad (17)$$

56 Finally, when combining eqns. 13-16 and setting  $K_{sa} = \frac{0.087 R_b g \rho_r Y}{k_v \sigma_T^2}$  we obtain for the erosion rate:

$$\dot{E}_f^{sa} = K_{sa} \frac{q_{sf}^\psi}{W} F_e [\tau^*/\tau_c^* - 1]^{-0.52} \left[ 1 - (u^*/w_f)^2 \right]^{1.5} \quad (18)$$

57 We compute the total erosion rate by summing the erosion rate of the individual sediment grain size bins (Table  
 58 S2):

$$\dot{E}_f^{sa} = \sum_{\psi=0}^8 K_{sa} \frac{q_{sf}^\psi}{W} F_e [\tau^*/\tau_c^* - 1]^{-0.52} \left[ 1 - (u^*/w_f)^2 \right]^{1.5} \quad (19)$$

59 In agreement with the sediment transport rules, we use  $\tau^* = \tau_s^*$  and  $\tau_c^* = \tau_{sc}^*$  for  $\psi = 0 - 1$ . For  $\psi = 2 - 8$ ,  
 60  $\tau^* = \tau_g^*$  and  $\tau_c^* = \tau_{gc}^*$ . The settling velocity,  $w_f(\psi)$ , is allowed to vary with grain size,  $D(\psi)$ , according to  
 61 Eqn. 17.

62 We assume that abrasion always produces new sediment with smaller grain size than the abrasive grains. The  
 63 new sediments produced by saltating sediments in bin  $\psi_i$  are therefore equally distributed across bins  $\psi_j < i$ . We  
 64 note that this leads to a natural downstream fining of average grainsizes.

**65 4 Supplementary discussion section****66 4.1 On the distribution of threshold slopes**

67 In the steady state configuration of the models presented in Fig. 1, bedrock landsliding represents a primary  
68 erosion mechanism because hillslopes are allowed to reach threshold slopes in many places. Yet, the threshold  
69 slopes are more widely distributed in the saltation-abrasion model (Fig. 1B), where critical threshold slopes are  
70 reached even for uplift rates smaller than  $0.1 \text{ mm yr}^{-1}$ . Local relief is therefore more independent of tectonic  
71 uplift rate in the saltation-abrasion model. This derives from the fact that fluvial incision by saltation-abrasion  
72 can decrease on steep slopes as the slopes increase, because the steeper gradient results in a dramatic drop in  
73 impact frequency, which significantly lowers the incision rate (19, 27, Fig. S2, Fig. S3). The fluvial erosion  
74 rate may therefore continue to decrease as the channel slope increases until threshold conditions are reached.  
75 At this point, landslide mechanisms are activated and become the dominant factor controlling the topographic  
76 gradient.

**77 5 Caption for supplementary movie S1**

**78 Movie S1:** The movie shows the landscape of a model simulation with river incision by saltation-abrasion,  
79 bedrock landslides, long-term regolith production on hillslopes, and sediment transport in rivers and on hill-  
80 slopes. Although the movie sequence captures the model landscape when in steady-state (i.e. erosion is gen-  
81 erally balanced by tectonic rock uplift), the topography is highly dynamic, showing rapid oscillations owing to  
82 feedbacks between landsliding and river incision. The yellow colors represent alluvial sediment that is caught  
83 in the fluvial drainage system because of dams generated by landslide deposits.

84

85 **References**

- 86 [1] Sklar, L. S. & Dietrich, W. E. A mechanistic model for river incision into bedrock by saltating bed load.  
87 *Water Resources Research* **40**, W06301 (2004).
- 88 [2] Sklar, L. & Dietrich, W. Implications of the saltation-abrasion bedrock incision model for steady-state  
89 river longitudinal profile relief and concavity. *Earth Surface Processes and Landforms* **33**, 1129–1151  
90 (2008).
- 91 [3] Hovius, N., Stark, C. P. & Allen, P. Sediment flux from a mountain belt derived by landslide mapping.  
92 *Geology* **25**, 231–234 (1997).
- 93 [4] Hovius, N., Stark, C. P., Hao-Tsu, C. & Jiun-Chuan, L. Supply and removal of sediment in a landslide-  
94 dominated mountain belt: Central Range, Taiwan. *The Journal of Geology* **108**, 73–89 (2000).
- 95 [5] Turowski, J. M., Hovius, N., Meng-Long, H., Lague, D. & Men-Chiang, C. Distribution of erosion across  
96 bedrock channels. *Earth Surface Processes and Landforms* **33**, 353–363 (2008).
- 97 [6] Wilcock, R. R. Toward a practical method for estimating sediment-transport rates in gravel-bed rivers.  
98 *Earth Surface Processes and Landforms* **26**, 1395–1408 (2001).
- 99 [7] Parker, G. & Andrews, E. D. Sorting of bedload sediment by flow in meander bends. *Water Resour. Res.*  
100 **21**, 1395–1408 (1985).
- 101 [8] Wilcock, P. R. Two-fraction model of initial sediment motion in gravel-bed rivers. *Science* **280**, 410–412  
102 (1998).
- 103 [9] Gasparini, N. M., Tucker, G. E. & Bras, R. L. Downstream fining through selective particle sorting in an  
104 equilibrium drainage network. *Geology* **27**, 1079–1082 (1999).
- 105 [10] Bitter, J. G. A. A study of erosion phenomena, part i. *Wear* **6**, 5–21 (1963).
- 106 [11] Rubey, W. W. Settling velocities of gravel, sand, and silt particles. *American Journal of Science* **25**,  
107 325–338 (1933).
- 108 [12] Baldwin, J. A., Whipple, K. X. & Tucker, G. E. Implications of the shear stress river incision model for  
109 the timescale of postorogenic decay of topography. *Journal of Geophysical Research* **108**, 2158 (2003).